Nanoscale

Accepted Manuscript

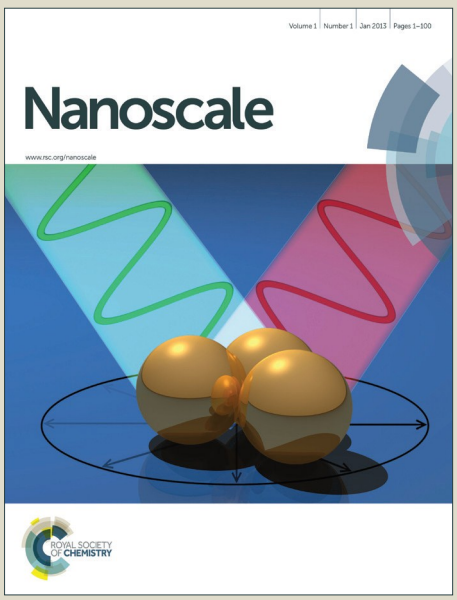

ROYAL SOCIETY OF CHEMISTRY

www.rsc.org/nanoscale

Journal Name

ARTICLE

Gene delivery nanocarriers of bioactive glass with unique potential to load BMP2 plasmid DNA and to internalize into mesenchymal stem cells for osteogenesis and bone regeneration

Received 00th January 20xx,
Accepted 00th January 20xx

DOI: 10.1039/x0xx00000x

www.rsc.org/

Tae-Hyun Kim[a,b,*], Rajendra K. Singh[a,b,*], Min Sil Kang[a,b], Joong-Hyun Kim[a,b], Hae-Won Kim[a,b,c,+]

Recent development of bioactive glasses with nanoscale morphologies has spurred their specific applications in bone regeneration, such as drug and gene delivery carriers. Bone engineering with stem cells genetically modified with this unique class of nanocarriers thus holds great promise in this avenue. Here we report the potential of the bioactive glass nanoparticle (BGN) system for the gene delivery of mesenchymal stem cells (MSCs) targeting bone. The composition of 15%Ca-added silica, proven to be bone-bioactive, was formulated into a mesoporous nanosphere with a pore size enlarged and a surface aminated, to effectively load and deliver bone morphogenetic protein-2 (BMP2) plasmid DNA. The enlarged mesopores were highly effective in loading BMP2-pDNA with an efficiency as high as 3.5 wt% (pDNA w.r.t. BGN), a level more than twice for the case in small-sized mesopores. The BGN nanocarriers could release the genetic molecules in a highly sustained manner (as long as 2 weeks). The BMP2-pDNA/BGN complexes were effectively internalized to rat MSCs with a cell uptake level of ~73%, and a major of cells were transfected to express the BMP2 protein. Subsequent osteogenesis of the transfected MSCs was demonstrated by the expression of bone-related genes, including bone sialoprotein, osteopontin, and osteocalcin. The MSCs transfected with BMP2-pDNA/BGN were locally delivered inside of collagen gel to the target calvarium defects. Results showed significantly improved bone regeneration, as evidenced by the micro-computed tomographic, histomorphometric and immunohistochemical analyses. This study supports the excellent capacity of the BGN as a pDNA-delivery nanocarrier in MSCs, and the engineered system, BMP2-pDNA/BGN with MSCs, may be considered a new promising candidate to advance the therapeutic potential of stem cells through a genetic modification, targeting bone defects and diseases.

Introduction

Bioactive glasses, over the last 40 years, have shown immense impacts on the regeneration of calcified tissues like bone and dentin, and even on soft tissues like muscle, tendon and ligament[1-7]. This enabled key bone forming mechanisms to be elucidated and a number of formulations to be clinically-available [8-13]. One of the most recent intriguing research inputs on this is the development of nano-scaled bioactive glasses, either in the form of nanofibers and nanoparticulates[14-19]. This is aimed to reap up the excellent compositional merit of the bioactive glasses as well as the morphological asset of the nanoscale domain that provides nanotopological cues for cellular anchorage or permits effective cellular entry of the nano-sized carriers.

The nanoparticulate form of bioactive glasses gains special interest for the delivery of therapeutic molecules into cells. Some recent studies have highlighted the potential of the bioactive glass nanoparticles (BGNs) in the delivery of small drug and genetic molecules[9,19-23], opening the new avenue of their uses as delivery systems. The currently developed BGNs are comprised mainly of silica (SiO_2) random networks, and the incorporated calcium (and other) ions at certain levels. Furthermore, the sol-gel process, generally used to produce BGNs, creates highly organized mesopores within the glass structure, with tunable mesopore properties including pore size, shape, arrangement, and porosity[11,17,24]. Therefore, the main feature of BGNs shares in common with the conventional mesoporous silica nanoparticles (MSNs). The potent ability of MSNs in homing biological molecules like antibiotic drugs and protein, and deliver them into the intracellular compartments, has been researched in vitro [25-30]. In those studies, the role of mesopore properties such as pore size, volume and surface area, were highlighted in determining the loading and delivery capacity.

[a] Department of Nanobiomedical Science and BK21 PLUS NBM Global Research Center for Regenerative Medicine, Dankook University, Cheonan 330-714, Republic of Korea.
[b] Institute of Tissue Regeneration Engineering, Dankook University, Cheonan 330-714, Republic of Korea.
[c] Department of Biomaterials Science, College of Dentistry, Dankook University, Cheonan 330-714, Republic of Korea.
* These authors contributed equally to this work
† Corresponding author: Tel: +82 41 550 3081; Fax: +82 41 550 3085; E-mail: kimhw@dku.edu

One of the most significant differences between BGNs and MSNs is the incorporated calcium ions within the glass chemistry; thus the possible biological properties, like the calcium ion release, and the degradation (or the induction of bone mineral-like phase) should be importantly considered. Furthermore, the therapeutic potential of BGNs through the incorporation of ions needs to be additionally yet vitally considered; the ions can vary in a wide range and elicit significant effects on the cellular functions, like cell proliferation, angiogenesis and osteogenesis[31-33]. The more degradable nature of the ionic-modified BGNs, with respect to MSNs, favors the clinical availability without a significant concern on the in vivo distribution and toxicity of the synthetic nanomaterials. Moreover, when we consider the target use of BGNs for mineralized tissues like bone and dentin, the BGNs can be a sort of nano-seeds that provide biochemical ionic sources to cells in their calcium phosphate mineralization, a terminal stage of cellular osteogenesis.

Although the potential of BGNs is immense, the studies on this unique class of nanomaterials are still in its infancy. Therefore, here we aim to demonstrate the efficacy of the BGNs for the delivery of biomolecules targeting bone. In particular, bone morphogenetic protein 2 (BMP2) plasmid DNA (pDNA) is delivered through BGNs into mesenchymal stem cells (MSCs), to stimulate their differentiation into an osteogenic lineage and ultimately bone regeneration. In fact, BMPs are special bone growth factors that induce the formation of bone and cartilage, and among them, BMP2 and BMP7 have high ossification activities and are used extensively in bone repair[34-36]. While the BMP gene delivery systems have been developed, including those utilizing MSNs, cationic lipids, and synthetic and natural polymers[37-41], there is no report on the utilization of BGNs for the genetic delivery into MSCs. Compared to other delivery systems, the merits of BGNs are considered particularly for hard tissues because the composition is favorable for bone cells, tunable with target ions, and possible to degrade *in vivo*.

For the effective loading and delivery of BMP plasmid, we first optimize BGNs with properties of large mesopore size and positive-charged surface. The BMP2-pDNA is designed to function within the cytosol by the interaction of RNA polymerase in the cytoplasm of the transfected cells. When the RNA polymerase meets the BMP2-pDNA, they initiate the process of BMP2 gene transcription and regulation of gene expression. We demonstrate the potential of the BMP2-pDNA/BGN delivery system in terms of i) loading and release ability of the genetic molecules, ii) cellular uptake and transfection efficiency, iii) osteogenesis of rMSCs, and iv) in vivo bone formation. The results will inform the potential usefulness of BGNs as a gene delivery nano-platform for bone repair and regeneration.

Experimental section

Preparation of BGNs with tailored mesoporosity

Among the mesopore parameters, the pore size of the BGNs was tailored to load pDNA. The large pore sized BGN (BGN(L)) was prepared in basic solution at room temperature using water, ethanol, and ethyl ether as co-solvents, and hexadecyltrimethylammonium bromide (CTAB) as a surfactant. In a typical procedure, 1 g of CTAB was dissolved in an emulsion system composed of 150 mL of H_2O, 2 mL of aqueous ammonia, 40 mL of ethyl ether, 20 mL of ethanol, and calcium nitrate tetrahydrate ($Ca(NO_3)_2{\cdot}4H_2O$). After the mixture was vigorously stirred at room temperature for 30 min, tetraethyl orthosilicate (TEOS) was quickly dripped into the mixture. The molar ratio of Ca/Si is 15/85. The resulting mixture was vigorously stirred at room temperature for 4 h. A white precipitate was obtained, filtered, washed with distilled water, and dried in air at 60 °C for 24 h and then calcined at 550 °C for 5 h to remove any remaining CTAB. The small pore sized BGN (BGN(S)) were synthesized by using CTAB as the surfactant and 2-ethoxyethanol as the co-solvent. In a typical procedure, 1 g of CTAB was dissolved in 150 mL of H_2O, followed by an addition of 2 mL of ammonia solution (25−28%), 40 mL of 2-ethoxyethanol and $Ca(NO_3)_2.4H_2O$. After TEOS was added dropwise into the solution, the mixture was vigorously stirred in a closed vessel for 4 h. A white precipitate was obtained, filtered, washed with distilled water, and dried at 60 °C. CTAB and other organic components were removed by calcination in air at 550 °C for 5 h.

The surface of BGNs was further amine-functionalized with (3-aminopropyl)triethoxysilane (APTES) for selective use in the gene delivery. BGN samples of 0.1 g of were added to 50 mL of toluene and sonicated for 30 min to a homogeneous solution. One milliliter of APTES was added to this solution and then refluxed at 80 °C for 24 h, which was followed by a centrifugation at 8000 rpm for 5 min and stringent washing with toluene and ethanol. The product was dried in an oven at 80 °C for 24 h.

Characterizations of BGNs

The crystalline phase of the samples was determined by X-ray diffraction (XRD; Ragaku). The samples were scanned in the range of diffraction angle 2θ = 5-60° at a rate of 2° min-1 with a step width of 0.02° 2θ using Cu Kα1 radiation at 40 kV and 40 mA current strength. Fourier transform infrared spectroscopy (FT-IR; Varian 640-IR) was used to determine chemical bond status of the samples. For each spectrum, 20 scans in the wave number of 400-4000 cm^{-1} were recorded in the transmission mode by potassium bromide (KBr) pellet method. The mesoporosity of the samples, including specific surface area and pore volume, were determined by N_2 gas adsorption/desorption using Brunauer–Emmett–Teller (BET) method. The pore size distribution was obtained by the Barret-Joner-Halenda (BJH) method. The morphology of the samples was characterized by transmission electron microscopy (TEM, JEOL-7100). The zeta (ζ) potential of the samples was measured using a Malvern Zetasizer (ZEN3600; Malvern). The ζ-potential was measured in triplicate at 25°C in deionized water.

Cell viability assay

For the cell viability assay of the developed BGNs, a series of cells were used. Rat adrenal medulla derived cell line (PC12), human cervical cancer cell line (HeLa), mouse macrophage cell line (RAW 264.7) and mouse osteoblast precursor cell line (MC3T3-E1) were purchased from the American Type Culture Collection (ATCC; Rockville, MD). The bone marrow derived rat MSCs and the rat dental pulp derived stem cells (rDPSC) were harvested from male adult Sprague-Dawley rats (4–5 weeks old, 180–200 g), according to code of practice for the care and use of animals for scientific purposes approved by Animal Ethics Committee, Dankook University. All cells were maintained at 37°C in an atmosphere of 5 % CO_2 in DMEM cell culture media containing 10 % FBS and 1% penicillin–streptomycin. The medium was replaced twice a week and the cells were passaged at sub-confluency.

First, rMSCs were plated in each well of 96-well culture plates at a density of 1 x 10^4 cells per well, and stabilized for 24 h. The culture medium was refreshed with that containing BGNs at a series of concentrations (0, 10, 20, 40, 80, and 160 μg/ml), cultured for 1, 3, and 7 days, and the cell viability was analyzed using a CCK-8 cell counting kit (Dojindo, Japan). 10 μL of CCK-8 solution was mixed with 100 μL of DMEM, which was added to each well, and then incubated at 37°C for 4 h according to the manufacturer's instructions. After incubation, 100 μL of each cell culture supernatant was collected, and the absorbance was measured at 450 nm using an iMark microplate reader (BioRad, USA). The absorbance values were normalized to those of control free of BGNs for each test group, and the data were averaged from triplicate samples (n = 3). For other types of cells (rDPSCs, PC12, MC3T3-E1, RAW264.7, and HeLa), the cell viability for 1 day was also analyzed using the same protocols.

Construction of GFP fusion BMP2 pDNA and purification

The GFP-fused BMP pDNA was prepared as described previously[28]. In brief, A BMP2 construct (283–396 amino acids) was generated by polymerase chain reaction (PCR) amplification of human BMP2 using the primers 5'-GAAGATCTGCCAAACACAAACAGCGG-3' and 5'-AACTGCAGATCTGTCTTTTCTACCGCTGGACACCCACAACCCTC-3'. The PCR product was in-frame ligated into the multiple cloning sites of pBAD/His (Invitrogen, USA), giving rise to a construct (pBAD/His-BMP2). A GFP fusion construct of BMP2 (pBAD/His-GFP-BMP2) was generated by PCR amplification of GFP from the pEGFP-NA (Clontech, Japan) using the primers 5'-AGAATTCTGAGCAAGGGCGAGGAG-3' and 5'-AAGAAGCTTCTACTTGTACAGCTCGT-3'. The amplified product was cloned into the *Eco*RI and *Hind*III sites of the pBAD/His-BMP2, giving rise to the construct pBAD/His-GFP-BMP2 (BMP2-pDNA).

Loading and release assays of BMP2-pDNA

The loading efficiency of the BMP2-pDNA onto the developed BGNs was analyzed. 1 μg of BMP2-pDNA was mixed with 10, 20, 40, 80 and 160 μg of the BGNs (pDNA:BGN = 1:10, 1:20, 1:40, 1:80 and 1:160) in 200 μL of PBS for 1 h in order to find the optimal mixing ratio based on the loading efficiency. The BMP2-pDNA and BGN mixtures were then centrifuged at 8,000 rpm at 4°C for 10 min to sediment down of the BMP2-pDNA loaded BGNs. After the centrifugation, only the free BMP2-pDNA unloaded onto BGNs were remained in the supernatant. The supernatant was gathered carefully, and the quantity of free BMP2-pDNA was assessed using a Nanodrop 2000 spectrometer (Thermo Scientific, USA). Based on this, the loading amount of BMP2-pDNA was calculated by the difference of the total BMP2-pDNA amount and the unloading free BMP2-pDNA amount. Next, to find the saturation amounts of the BMP2-pDNA loading onto BGNs, varying concentrations of BMP2-pDNA (0.1, 0.25, 0.5, 1.0, 1.5 and 2.0 μg) was mixed with 10 μg of BGNs for 1 h at room temperature, and the BMP2-pDNA loading levels were analyzed as previously described

To study the BMN2-pDNA release behaviors from the BGNs, the BMP2-pDNA/BGN complexes were prepared with 1 μg of BMP2-pDNA and 80 μg of BGNs, mixing in 200 μL of PBS for 1 h at room temperature, followed by centrifugation at 8,000 rpm at 4 ºC for 10 min. The supernatants were then removed carefully and the pelleted complexes were resuspended in 200 μL of PBS and incubated at 37 ºC for different time points. At each time point, the samples were centrifuged and the supernatant was gathered for the measurement of the released BMP-pDNA amount by the Nanodrop spectrometer. After the assay, the pallets were resuspended for the next run.

Gene complexation assay

The BMP2-pDNA complexation with the BGNs was investigated by means of an agarose gel electrophoresis. The agarose gels were made at a concentration of 1.5 % (w/v) in Tris-acetate-EDTA buffer (pH 8.0) and contained 0.5 μg/mL ethidium bromide. The complexes made at different BMP2-pDNA : BGN ratios (1:10, 1:20, 1:40, and 1:80), and the agarose gel electrophoresis was applied at 100 V for 20 min. Free BMP2-pDNA was used as control, and the pDNA band images were captured using a GBOX-EF gel documentation system (Syngene, UK).

Uptake into rMSCs

For the cellular internalization of the BM2-pDNA/BGN complexes, the rMSCs were seeded at 1x10^5 cells on each well of 6-well culture plates and incubated for 24 h. The BMP2-pDNA/BGN complexes, prepared from the mixture of 1 μg of BMP2-pDNA with 80 μg of BGN in 1 mL of Opti-MEM transfection medium (Invitrogen) for 1 h, were added to each well. After 4 h of incubation, the medium was removed and cells were washed with PBS. The cells were then harvested or cultured in DMEM until used in the next experiments. The harvested rMSCs after the BMP2-pDNA/BGN treatment for 4 h were fixed in 4% paraformaldehyde solution for 30 min on the coating slide glass and washed twice with cold PBS for 5 min. Then, the GFP signals of BMP2-pDNA/BGN in the transfected cells were observed and analyzed by confocal laser scanning microscopy (CLSM; LSM 510, Carl Zeiss, Germany). The nuclei

of rMSCs were counterstained with 4',6-diamidino-2-phenylindole (DAPI; Invitrogen) and expressed as blue signals. For the quantification of intracellular uptake efficiency of the BMP2-pDNA/BGN, the expression of GFP signals in the harvested and fixed rMSCs were determined using a FACSCalibur flow cytometer (BD Biosciences, USA). The data acquired for 10,000 cells in each sample were analyzed using the CellQuest Pro software (BD Biosciences). Comparison groups including non-treated cells, free BMP2-pDNA, and BGN-treated cells were also tested.

Intracellular localization by TEM observation

For TEM observation, the cells treated with BMP2-pDNA/BGN were harvested and fixed in a mixture of 2% paraformaldehyde and 2.5% glutaraldehyde with 0.2 M PBS for 12 h at pH 7.2. Post-fixation was conducted using 1% osmium tetroxide in PBS for 2 h. Subsequently, the fixed cells were dehydrated in ascending concentrations of ethanol (70, 80, 90, 95, and 100%) and embedded in EMbed 812 resin (EMS, USA) using propylene oxide. Ultrathin sections were obtained from an ultramicrotome (Leica, USA), and were double stained with uranyl acetate and lead citrate. The stained sections were mounted on the grids and then examined with a H7000 microscope (Hitachi, Japan) operating at 80 kV.

Endogenous BMP2 expression by rMSCs

After the treatment with BMP2-pDNA/BGN for 4 h, the rMSCs were cultured for 24 h and 48 h and then harvested for the transfection assay by means of an endogenous expression of BMP2. The non-treated control rMSCs and the rMSCs treated with empty vector loaded BGN (EV/BGN) were also cultured under the same conditions for comparison purpose. The empty vector has the same construction as the one used in BMP2 plasmid. The harvested cells of each experiment group were fixed in 4% paraformaldehyde, incubated with anti-BMP2 antibody (Santa Cruz Biotechnology, USA) for 12 h at 4^{o}C, washed with PBS, and then incubated with Alexa Fluor 546 conjugated secondary antibody (Invitrogen) for 2 h in dark condition. The stained cells were then analyzed using a FACSCalibur flow cytometer to quantify the population of cells that expressing BMP2 signals. The data acquired for 10,000 cells in each sample were analyzed using the CellQuest Pro software (BD Biosciences).

Osteogenic gene expression by quantitative RT-PCR

After the BMP2-pDNA/BGN treatment, rMSCs were cultured for 14 days, and the expressions of osteogenic genes, including bone sialoprotein (BSP), osteopontin (OP), and osteocalcin (OC), were confirmed by quantitative real-time RT-PCR. The first strand cDNA was synthesized from the total RNA (2 μg) using a SuperScript first strand synthesis system for real-time PCR (Invitrogen) according to the manufacturer's instructions. Real-time PCR was conducted using SYBR qPCR SuperMix reagents (Invitrogen) and a Bio-Rad iCycler. The relative transcript quantities were calculated using the ΔΔCt method with the gene encoding glyceraldehyde 3-phosphate dehydrogenase (GAPDH) as the endogenous reference gene amplified from the samples. Primer sequences were as follows: BSP forward: 5'-AGAAAGAGCAGCACGGTTGAG-3', reverse 5'-TCATAGCCATGCCCCTTGTAG-3'; OP forward 5'-GAGGAGAAGGCGCATTACAG-3', reverse 5'-AAACGTCTGCTTGTGTGCTG-3'; OC forward 5'-AGCTCA ACCCCA ATTGTG A-3', reverse 5'-AGCTGTGCCGTCCATACTTT-3'; GAPDH forward 5'-AAACCCATCACCATCTTCCA-3', reverse 5'-GTGGTTCACACCCATCACAA-3'

In vivo bone regeneration model

Rat calvarium critical-sized defect model was used for the *in vivo* bone regeneration effects of the BMP2-pDNA/BGN delivery system. All the experimental procedures were reviewed and approved by the Animal Care and Use Committee, Dankook University, Republic of Korea. Surgery was performed under general anesthesia with intramuscular injection of ketamine (80 mg/kg) and xylazine (10 mg/kg). The surgery area of the cranium in each rat (eleven weeks old male Sprague-Dawley rats, Daehan Biolink Co., Ltd, Korea) was shaved, and the surgical field was aseptically prepared. The cranium surface was exposed by a skin incision and the periosteum elevation. A full-thickness critical-sized circular calvarial bone defect was created bilaterally by using a 5 mm diameter trephine bur without damaging the underlying sagittal sinus and dura matter, under the extensive irrigation with normal saline. Experimental groups were prepared as follows: rMSCs treated with EV/BGN, and rMSCs treated with BMP2-pDNA/BGN, both of which were encapsulated within a collagen gel matrix. Collagen gel without cells and empty defect control were also used for comparison purpose. Each defect was divided randomly for the implantation of the samples. After the implantation, the subcutaneous tissue was closed with absorbable materials, and skin flap was sutured with 4-0 Prolene (Ethicon, Germany). The animals were housed individually and monitored. Animals were maintained in a barrier system with controlled environment, and allowed normal diet and water ad libitum. The animals were sacrificed at six weeks after operation, and the calvarial portion surrounding the drill hole was harvested with its surrounding tissues. The harvested specimens were immersed in 10% buffered neutralized formalin for 1 day and were used for further analyses.

Micro-computed tomography

Following fixation, the samples were prepared for the micro-computed tomography (μCT) analysis of new bone formation. μCT imaging was performed using Skyscan 1176 (Skyscan, Aartselaar, Belgium). The X-ray tube voltage was 65 kV and the current was 385 μA, with an exposure time of 279 ms. After the μCT data were reformatted, the new bone formation in the defect was calculated. Moreover, the three dimensional μCT images with a threshold adjusted to remove the soft tissue signals were prepared by a μCT imaging program, CTAn (Skyscan).

Histology and bone histomorphometric analysis

After the μCT imaging, the harvested samples were used for further histomorphometric analysis. The samples were decalcified with RapidCalTM solution (BBC Chemical Co., Stanwood, WA). After this, the samples were dehydrated and embedded in paraffin using standard procedures. Five serial sections (5 μm) were cut at the central of the defects, and the deparaffinized sections were subjected to hematoxylin & eosin (H&E) and Masson's trichrome (MT) stains, and then imaged using a light microscope. For the bone histomorphometric analysis, the structural parameters (% bone length and % bone area) were analyzed from the defect area. The nomenclature, symbols, and units used were those recommended by Parafitt et al.

In vivo immunohistochemical assay

For immunohistochemical staining of the *in vivo* samples, the deparaffinized sections were washed three times in PBS. Nonspecific binding sites were blocked by incubating sections in 3% hydrogen peroxide for 20 min at room temperature, and then the sections were incubated overnight at 4°C with anti-BMP2, anti-osteocalcin, and anti-osteopontin antibodies (Santa Cruz Biotechnology, CA, USA) at 1:100. After rinsing in PBS, the sections were incubated in biotinylated anti-rabbit or anti-goat IgG secondary antibody (Santa Cruz Biotechnology) in a humidified chamber for 1 h at room temperature. Positive immunoreactivity was detected with drops of streptavidin conjugated to horseradish peroxidase, and the peroxidase activity was visualized using 3-3'-diaminobenzidine (DAB) as the substrate. The sections were counterstained with hematoxylin, and the photomicrographs were acquired and analyzed.

Statistical analysis

Data were expressed as the mean ± standard deviation (SD), and statistical comparison among groups was carried out by one-way analysis of variance (ANOVA) with a *P*-value < 0.05 considered statistically significant.

Results and discussion

BGNs developed for the delivery system

The synthetic procedures to prepare different pore sizes of BGNs are schematically illustrated in **Fig. 1.** The use of co-solvent ethyl ether is critical to obtain large pores due to the gasification of the volatile solvent (boiling point as low as 34°C), which is contrasted to the case for using 2-ethoxyethanol employed for conventional small-pored nanoparticle[42,43]. While both ethyl ether and 2-ethoxyethanol have only slight difference in their chemical structure, these two molecules have significantly different boiling points, which primarily contribute to change in the pore development[42]. On detailing the mechanism of large-pore generation, first is the micro-emulsion formation wherein a mixture of water, NH_4OH, CTAB, and ethyl ether coexist. Within this mixture, calcium and TEOS precursors are added, which further condensate and self-assemble on the surface of nano-droplets. Meanwhile, due to the nature of exothermic hydrolysis of calcium/silica precursors, ethyl ether with low boiling point (34°C) is highly volatile, escaping from the unstable emulsion, passing through the shell of condensed calcium/silica, and forming nano-channels with increased sizes. On the other hand, when 2-ethoxyethanol is added, it stabilizes the micelle formation of CTAB which interacts with negative-charged calcium/silica sol precursors through week interactions, and aids in polycondensation and mesopore generation, thus small-pored BGNs are generated.

The typical nanoscale morphologies of the BGNs were characterized by SEM and TEM. The SEM images show that uniform sized nanospherical particles are generated well, with a mean diameter approximately 100 nm (**Fig. 2a,b**). TEM images show the randomly developed large-sized mesopore structure in BGN(L) (**Fig. 2c**). The mesopore characteristics of the BGNs, including mesopore size, surface area, and pore volume, as analyzed by BET method, are summarized (**Table 1**). The BGN(L) show a specific surface area of 610~630 m^2/g, and a pore volume of 0.54~0.56 cm^3/g, and these values are comparable to those of BGN(S). However, the pore size is 6.4~6.9 nm, in striking contrast to 2.3~2.4 nm for BGN(S). The surface charge property of the BGNs was also characterized by a ζ-potential measurement, and the result gives +18.2~+18.4 mV which achieved through the amination process. The BGN(S) show a similar value (+19.1~+19.4 mV). Taken all, the BGNs developed herein possess high mesoporosity level (surface area and pore volume), large pores, and positive-charged surface, which is considered to be appropriate to deliver large genetic molecule, pDNA.

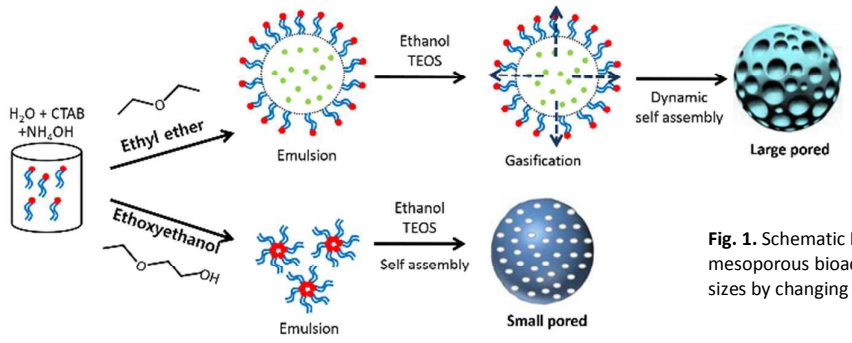

Fig. 1. Schematic Illustration of the structure-controlled formation of mesoporous bioactive glass nanoparticle (BGN) with different pore sizes by changing the co-solvent (ethyl ether or ethoxyethanol).

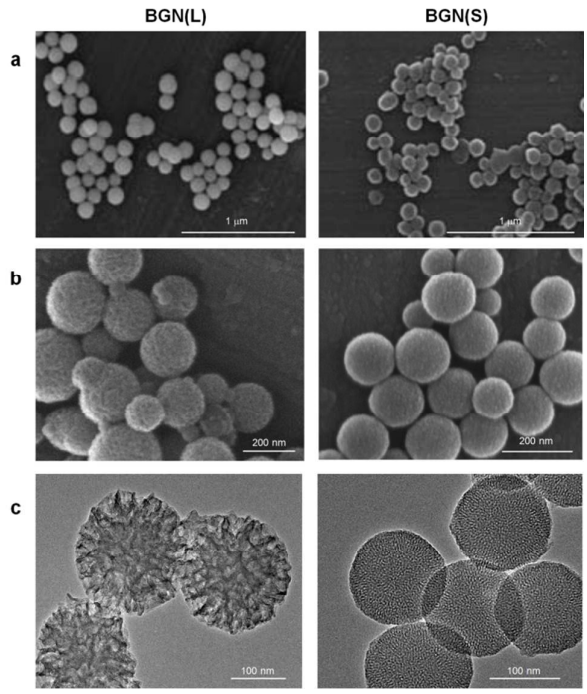

Fig. 2. (a,b) SEM and (c) TEM images of mesoporous bioactive glass nanoparticles with large (BGN(L)) and small pores (BGN(S)).

Table 1 Characteristics of mesoporous bioactive glass nanoparticles with large (BGN(L)) and small pores (BGN(S))

	BGN(L)	BGN(S)
Surface area (m^2/g)	600~610	620~630
Pore volume (cc/g)	0.54~0.56	0.40~0.48
Pore size, BJH (nm)	6.6~6.9	2.3~2.4
ζ-potential, before amination (mV)	-15.2~-15.3	-14.0~-14.1
ζ-potential, after amination (mV)	+18.2~+18.4	+19.1~+19.4

After confirming the physico-chemical properties, we assessed the cellular toxicity of the BGNs as a first criterion for the biological uses. The cytotoxic effects on rMSCs were examined at various doses (0, 10, 20, 40, 80, and 160 μg/mL). After 1, 3, and 7 days of culture of the cells with the BGN-treatment, the viability was assessed by a CCK method. Cells are highly viable for both types of BGNs over the doses ranged **(Fig. 3).** Supplementary results also show the viability level of different cell lineages, including rDPSCs, PC12, MC3T3-E1, RAW 264.7 and HeLa at day 1; the BGN samples show excellent viability levels for all cell types (**Fig. S1**). This excellent cell viability of the 15%Ca-added BGN composition has also been noticed elsewhere, and the nanoparticles have even been shown to stimulate the cellular viability when dosed properly, which were reasoned to be the possible ionic releases from the nanoparticles[2,10,44].

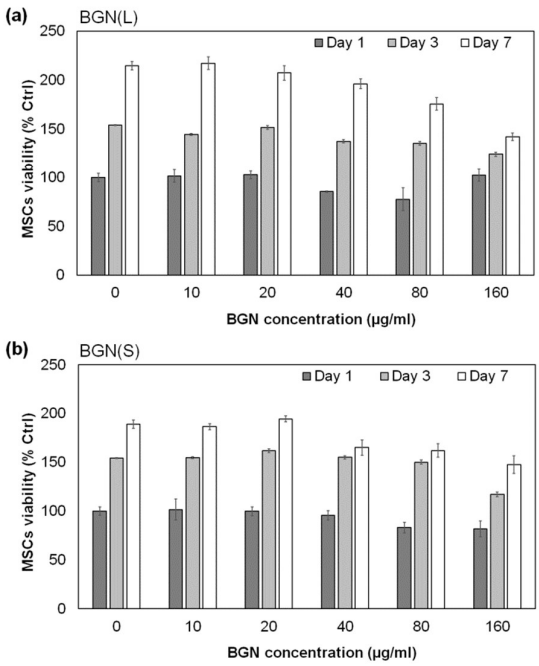

Fig. 3. Rat MSC viability assay of (a) BGN(L) and (b) BGN(S) using CCK-8 assay. Cells were treated with nanoparticles at various concentrations (0, 10, 20, 40, 80, and 160 μg/mL) for 1, 3 and 7 days. Data are normalized to the level of control medium without nanoparticles at day 1, and is shown as means ± standard deviations from three replicate tests.

Effective loading of BMP2-pDNA onto BGNs and the sustained release

To determine the optimal complexation conditions for BMP2-pDNA with the BGNs, the nanoparticles were mixed with BMP2-pDNA at varying ratios (1 μg of BMP2-pDNA mixed with 10, 20, 40, 80 and 160 μg of BGNs) for 1 h, and the loading amount of BMP2-pDNA was measured. Significantly higher loading amounts are recorded for BGN(L) when compared to BGN(S); 0.27, 0.45, 0.75, 0.91 and 0.99 μg of BMP2-pDNA onto BGN(L) vs. ~0.02, 0.15, 0.48, 0.67 and 0.72 μg of BMP2-pDNA onto BGN(S) (**Fig. 4a**), confirming the effective role of pore size in the loading of pDNA. Next, we determined the pDNA loading saturation dose for the BGNs. BGNs of 10 μg were mixed with BMP2-pDNA at varying contents (0.1, 0.25, 0.5, 1.0, 1.5, and 2.0 μg) for 1 h, and the pDNA loading amount was measured. The maximal loading amount of BMP2-pDNA recorded is 0.36 μg and 0.14 μg for BGN(L) and BGN(S), respectively (**Fig. 4b**), showing approximately 2.5 times increase in the loading capacity by the pore enlargement. The pDNA complexation with BGNs was further confirmed by an agarose gel electrophoresis (**Fig. 4c**). Different contents of BGN(L) were mixed with 1 μg of pDNA at pDNA:BGN ratios of 1:10, 1:20, 1:40 and 1:80. The lanes in the 1:10 and 1:20 of pDNA:BGN ratios show migrated pDNA bands in the agarose gel, indicating the existence of a certain level of un-complexed free pDNA. At 1:40, the band intensity of the free pDNA decreases substantially, and at 1:80 there is no band

expression, indicating almost all pDNA molecules are complexed with the BGNs. The BMP2-pDNA:BGN ratio of 1:80 is thus used in further experiments.

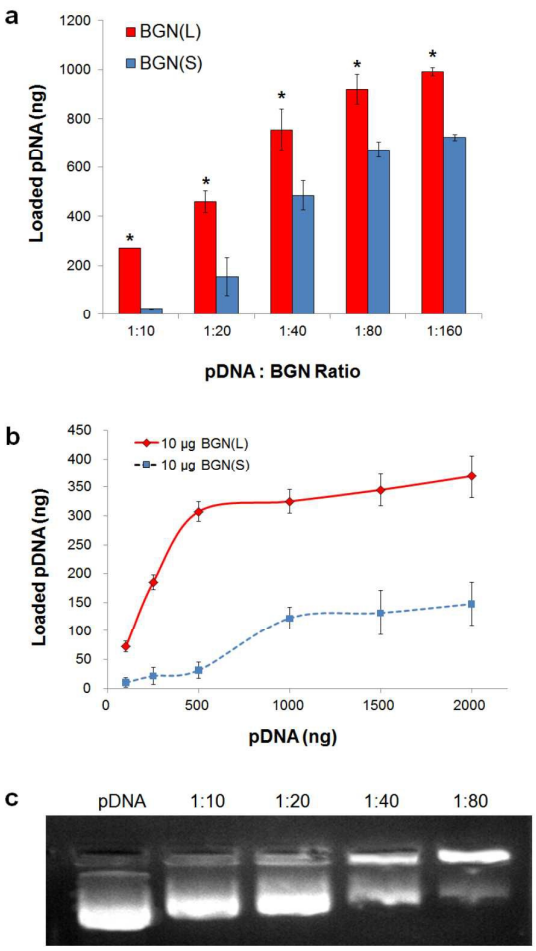

Fig. 4. BMP2-pDNA loading assays on the BGNs. (a) 1 μg of BMP2-pDNA was mixed with varying amounts of BGNs for 1 h. The loading efficiency was of 67.2 % for BGN(S) and 91.9 % for BGN(L) at a 1:80 ratio of BMP2-pDNA:BGN. (b) The loading amount plotted with respect to BMP2-pDNA content, which varied (0.1, 0.25, 0.5, 1.0, 1.5 and 2 μg) with a fixed 10 μg for the BGNs. The graph shows the loading saturation amounts of BMP2-pDNA for the BGN(S) and BGN(L). The loading amount is significantly higher for BGN(L) than for BGN(S) at all conditions. (c) Gel electrophoresis image showing the gel retardation property of BMP2-pDNA-BGN(L) complexes at different BMP2-pDNA:BGN(L) ratios (1:10, 1:20, 1:40 and 1:80). *statistical significance considered at $P < 0.05$.

The release profile of pDNA from BGNs was then investigated. The pDNA/BGN complexes were made at a ratio of 1:80, and the pDNA release patterns were monitored in PBS at 37°C for up to 17 days. Data are presented as both the cumulative amount (**Fig. 5a**) and the % of initial loading (**Fig. 5b**). From BGN(S), pDNA is released up to 7 days followed by a plateau; whereas pDNA release from BGN(L) continues up to 13 days, demonstrating the large-pored BGNs sustain the pDNA release more than a week. The release up to ~7 days, recorded to be similar for both BGNs (regardless of the different pore size), is considered to result from the pDNA bound to BGN through similar chemical interactions; on the other hand, the continual release after 7 days observed only for BGN(L) suggests the slow release of pDNA that is possibly loaded within the large pore channels. When the release amount is converted to the initial loading %, the total release corresponds to about 81-82 %, suggesting that about 18-19% of pDNA might be degraded during the test.

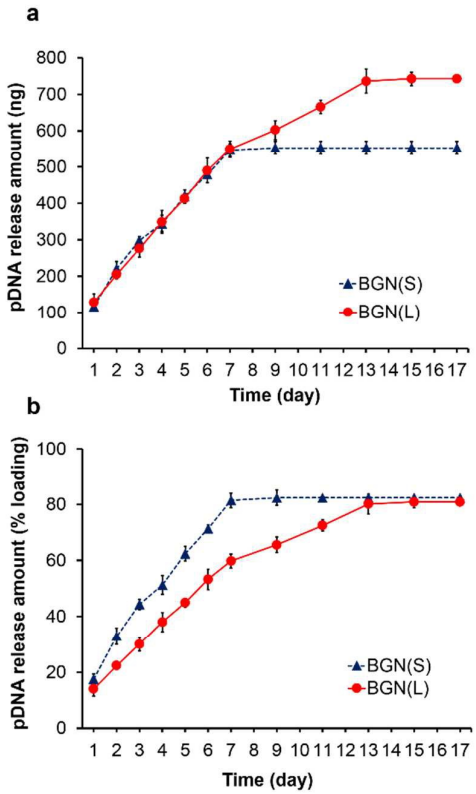

Fig. 5. *In vitro* release profile of pDNA from BGN(L) and BGN(S). (a) Cumulative release amount of pDNA and (b) release % of initial loading, recorded for up to 17 days. The pDNA release was almost completed at about the 7th day for BGN(S) and the 13th day for BGN(L). Three replicate samples were tested for each experiment.

Based on the results, the BGNs prove not only excellent loading capacity for pDNA but also its long-term release. The enlarged pore size is considered an important parameter to increase the loading capacity and to sustain the release of pDNA since both BGNs have similar mesopore properties like surface area and pore volume, except pore size. Unlike the small genetic molecules like siRNA that can be easily loaded onto BGN(S)[45], the pDNA has much larger size, thus requiring larger-pored carrier BGN(L).

The release of pDNA loaded within the mesopores of BGNs, is highly sustainable. Even from the small-pore nanoparticles, the loaded pDNA is released over a week, with almost a linear pattern. More importantly, the pDNA release from the large-pored BGNs is much more sustained, extending the complete release period as long as 2 weeks. It is considered that the

interaction between pDNA and the surface of BGN might be strong enough to sustain the liberation of genetic molecules over time. In our recent study, the release of small genetic molecule siRNA from the BGN was shown to complete ~3-4 days, not for such a long-term release[19,45]. It is thought that the large-sized pDNA molecules have much stronger interactions with the BGNs, probably due to the larger amount of negatively charged groups like phosphates in pDNA. The presence of calcium ions in the BGN amorphous structure can also form a sort of chemical interactions with the nucleic acids[46,47]. Furthermore, the larger sized pDNA might degrade less than siRNA, enhancing the detection sensitivity. Although the current observation was made in the *in vitro* acellular conditions (buffered saline), thus limits extrapolation to the phenomenon within cells, the results support the usefulness of BGN carriers as a delivery platform of genetic molecules to elicit therapeutic effects for a long-term period over weeks. This aspect is also particularly important in the current study, where the BMP2 molecules need to be produced quite continuously over a long time frame within cells in order to stimulate the osteogenic development of MSCs and the effective engagement in the *in vivo* bone regeneration[48,49].

Internalization of BMP2-pDNA/BGN into rMSCs and the osteogenic stimulation

The intracellular uptake efficiency of the BMP2-pDNA/BGN complexes was then determined by the GFP signalling that tagged in the BMP2-pDNA. For comparison purpose, cells treated with BMP2-pDNA (no carrier) only or with BGN only (no BMP) were also tested. Confocal microscopic images reveal that the rMSCs treated with BMP2-pDNA/BGN(L) clearly express the green GFP signals in the cytoplasm, whereas the cells treated with BMP2-pDNA only or BGN only show no fluorescence signals (**Fig. 6a**). The intracellular uptake level was then quantitatively analyzed by a flow cytometry, by sorting the cells positive for GFP signals. The BMP2-pDNA/BGN group show that about 72 % cells are positive for the signals, whereas other groups show no such positive signals (**Fig. 6b**). After the BMP2-pDNA/BGN delivery into cells, the intracellular ultrastructure was also observed by TEM. At low magnification, the cell organelles, such as nucleus (N) and endosomal vesicles (En) are shown to preserve well, and a higher magnification image reveal the presence of spherical nanoparticulates which are distributed profoundly in the cytoplasm (**Fig. 6c**).

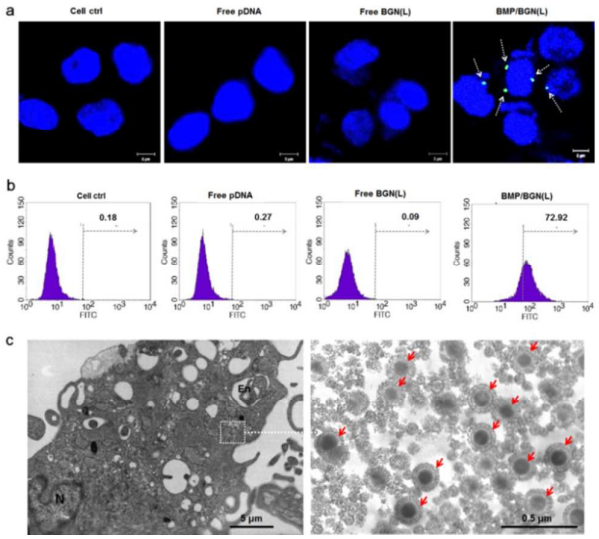

Fig. 6. Intracellular uptake efficiency of BGN(L) by rMSCs. (a) Confocal laser images cells following BMP2-pDNA/BGN(L) treatment for 4 h. BMP2-pDNA/BGN(L) treated cells only show GFP signals compared to control cells without treatment (Ctrl), cells treated with free BMP2-pDNA (Free pDNA) or free BGN(L). The nucleus of rMSCs was counterstained with DAPI in blue. Scale bar = 5 μm. (b) Intracellular uptake efficiency quantified by flow cytometry using GFP signals of BMP2-pDNA. (c,d) TEM ultrastructural images of BMP2-pDNA/BGN(L) treated cell. Nanoparticles are distributed and accumulated in the cytoplasm (indicated as arrows). Nucleus (N) and endosomal vesicle (En) are also visualized.

After confirming the cellular internalization of the delivery system, we next sought to find the induction of BMP2 protein due to the intracellular transfection. The rMSCs treated with the delivery system were cultured for 24 h, 48 h, and 72 h, and then the expression of BMP2 protein was analyzed by flow cytometry. The expression of BMP2 protein is only observed in the BMP2-pDNA/BGN treated cells, but not in the other groups like cell control without treatment, and empty vector/BGN treated cells (EV/BGN). The cells positive for BMP2 expression are as high as ~80 %, 91% and 83% at 24 h, 48 h, and 72 h, respectively, when transfected with the BMP2-pDNA/BGN delivery system (**Fig. 7a**). One thing to note is that the distribution of cells positive for BMP2 signals is relatively broad initially (24 h), not showing a sharp population, implying a heterogeneous population of cells that expressing BMP2 protein at different levels, which however, becomes more homogenous with increasing culture time from 24 h to 48 h and 72 h, suggesting the intracellular transfection process is also time-dependent, and this is also possible due to the effects of continuous BMP2-pDNA release from the BGNs within cells. The results demonstrate a majority of cells are transfected successfully, expressing induced BMP2 protein at substantial levels.

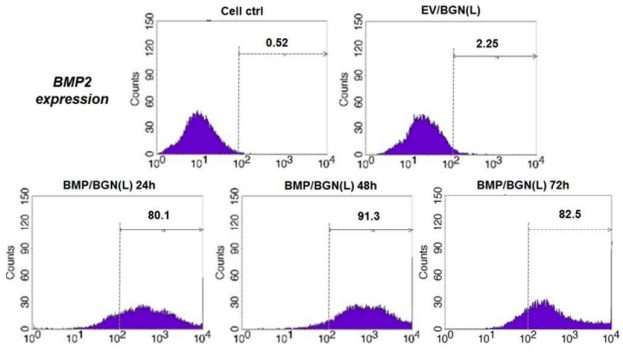

Fig. 7. Expression of BMP2 protein in BMP2-pDNA/BGN(L) treated rMSCs. After culture for 24, 48, and 72 h, cells were stained with anti-BMP2 antibody and Alexa fluor 546 conjugated secondary antibody. Cell fraction positive for BMP2 expression was analyzed by flow cytometry. Control cells (cell ctrl) and empty vector-loaded BGN(L) (EV/BGN(L)) treated cells are also tested.

Next, the osteogenesis of rMSCs after the BMP2 transfection was examined. The expression of representative bone-associated genes including BSP, OP, and OC, was analyzed by real-time RT-PCR at day 14 (**Fig. 8a**). All genes are expressed at significantly higher levels in the BMP2-pDNA/BGN transfected cells with respect to those in control cells without the transfection or in the cells treated with empty vector-loaded BGNs (increment is as high as 3.7 for BSP, 4.7 for OP, and 4.8 for OC). The ALP activity of cells at 14 days is also significantly higher on the cells following the BMP2-pDNA/BGN delivery (**Fig. 8b**). The protein expressions were also analyzed by FACS. The fraction of cells expressing ALP, OP or OC is much higher on the BMP-delivered system than on other groups (**Fig. 8c**), demonstrating stimulatory effects on the osteogenesis of rMSCs through the BMP2 gene delivery system.

The series of results clarified the performance of the BGNs as a promising non-viral tool to genetic regulation of MSCs. The pDNA-complexed BGNs are internalized into cells over 70% and lead to BMP2 expression in a majority of cells, which ultimately stimulates the stem cell differentiation towards an osteogenic lineage.

In fact, the gene delivery studies using other nanocarriers including MSNs, calcium phosphates and polymeric nanoparticles targeting bone have been shown to be effective for the osteogenesis of cells[38,50-53]. Although it is not easy to directly compare the BGN system with other studies, possibly due to the difference in cell type, target gene, and measurement tools, the performance of BGN *in vitro*, viz., excellent cell internalization, high transfection of BMP2, and sufficient expression of osteogenic markers, support the usefulness of the delivery system in stimulating MSCs for bone repair purposes.

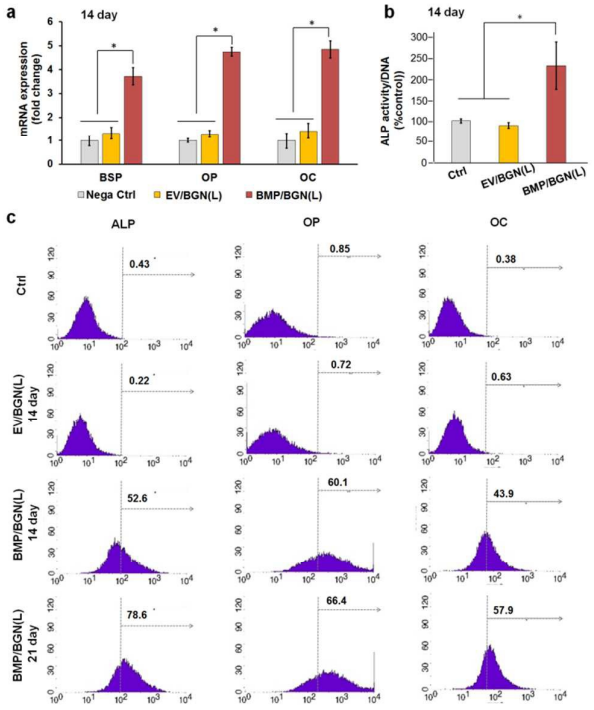

Fig. 8. Osteogenesis of rMSCs through the BMP2-pDNA/BGN(L) delivery system. (a) Expression of bone-related genes (BSP, OP and OC) analyzed by real-time RT-PCR, (b) ALP enzymatic activity, and (c) expression of proteins (ALP, OP and OC) analyzed by FACS. The BMP2-pDNA/BGN(L) treated cells for 4 h were cultured for 14 and/or 21 days and then analyzed. *statistical significance considered at $P < 0.05$.

Effects on in vivo bone regeneration

To investigate the efficacy of the gene delivery system and the transfected rMSCs for bone engineering we modelled critical-sized calvarial defects in SD rats. The rats had a recovery without infection through the study period. The scheme of the *in vivo* model and the assays for detection of bone formation is illustrated in the supplementary figure (**Fig. S2**). Two 5 mm-diameter defects created in the rat calvarium were implanted randomly with two of the four sample groups; empty defect ('Empty'), collagen gel only ('Gel'), collagen gel incorporating empty vector/BGN delivered rMSCs ('EV/BGN+MSC'), collagen gel incorporating BMP2-pDNA/BGN delivered rMSCs ('BMP/BGN+MSC'). Six weeks following surgery, tissue samples were harvested for the μCT analyses. Based on the 2D cross-sectional and 3D reconstructed images, the quantity and quality of newly formed bone were assessed. In particular, maximum intensity projection (MIP) images with color mapping, in conjunction with histological images, were also used to assess the bone formation, and the immunohistochemical assays were carried out to examine the *in vivo* secretion of bone matrix molecules.

Frist, the 3D μCT images are reconstructed to show the calcified bone tissue formation within the defects (**Fig. 9a**). In the empty control and Gel groups, there is minimal bone formation only at the marginal defect area. In contrast, the BMP/BGN+MSC group shows almost complete bone formation

in the defect. On the other hand, the EV/BGN+MSC group also appears to show a substantial bone formation at the central part of the defect. The quantification of µCT images, as indexed by the bone volume, bone surface area and surface density, further reveals the quantity and quality of newly formed bone (**Fig. 9b**). In the EV/BGN+MSC group, there are some increases in all of the bone formation indices when compared to the Gel group, implying that the gene-free BGN-treated rMSCs play some roles in the bone formation. In fact, the BGN composition itself can also be a stimulator for the osteogenic development of stem cells including MSCs, as deduced from previous studies[2,17,21,24,54]. For example, the rMSCs, in a collagen gel, can be stimulated by the release of ions from BGNs present around, to an osteogenic lineage[22]. However, compared to the stimulation by the BGN-treated rMSCs, the roles played by the BMP-induced genetic signalling are more substantial in the bone formation. The BMP/BGN+MSC group shows significantly enhanced bone formation with respect to EV/BGN+MSC group in all aspects; 54.4% vs. 31.9% for bone volume, 46.4 mm^2 vs. 30.8 mm^2 for bone surface area, and 6.9 mm^{-1} vs. 4.4 mm^{-1} for surface density. The results imply the importance of the osteogenic alteration of rMSCs in order to utilize the stem cells' capacity more effectively in the bone regenerative process; this event is primed by the genetic stimulation through BMP2-pDNA/BGN delivery system.

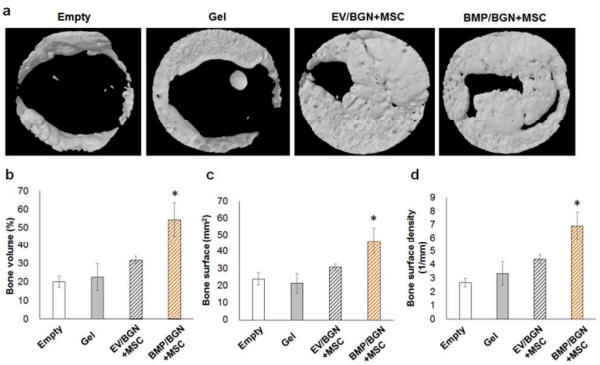

Fig 9. (a) 3D µCT images of the calvarial defect region of rat, and (b-d) image analysis data including bone volume, bone surface, and bone surface density. Data are the mean ± SD. Statistically significant difference noticed between the empty vector- and BMP-delivered groups (*P < 0.05).

Further, the 2D cross-sectional images are reconstructed, and the MIP images, together with the HE and MT stained histologic features, are presented (**Fig. 10a**). The color intensity mapping of the MIP images, as obtained by the µCT imaging program DataViewer, visualize the bone mineral density, and show a clear difference of the dense bone formation particularly at the central region of defect between BMP/BGN+MSC and EV/BGN+MSC groups. The HE & MT stain images are visualized to examine the bone structure histologically. For all groups, the surrounding tissues are in their native form, and no inflammation is observed. In the Empty and Gel groups, the defects are filled mostly with loose connective tissues, but with limited calcified tissues within the defect. However, new bone formation is clearly observed in the BMP/BGN+MSC and EV/BGN+MSC groups. A dense immature calcified tissue matrix fills the defect region almost completely in the BMP/BGN+MSC group. The histomorphometric analysis then quantifies the level of new bone length and new bone area; the new bone length is 35.3% for Empty < 34.3% for Gel < 74.0% for EV/BGN+MSC < 97.4% for BMP/BGN+MSC, and the new bone area is 25.0% for Empty ~ 20.6% for Gel < 57.5% for EV/BGN+MSC < 80.0% for BMP/BGN+MSC (**Fig. 10b**). Along with the 3D µCT constructed evaluations, the MIP- and histologic-based analyses clarify again the effects of the BMP-complexed BGNs on the bone formation quantitatively.

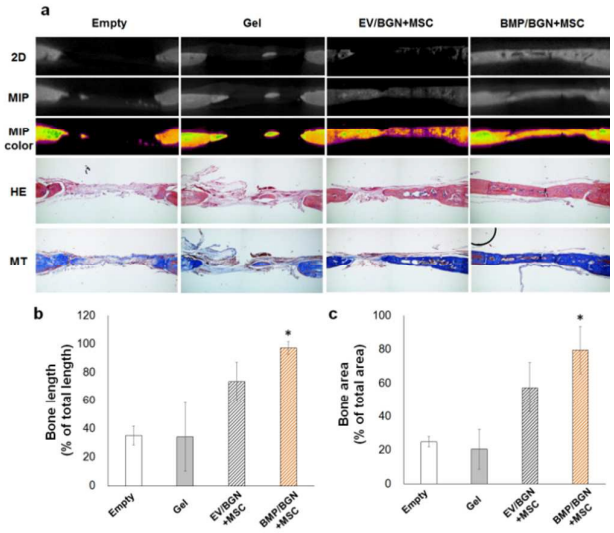

Fig. 10. (a) Maximum Intensity Projection (MIP) images with color mapping revealed for the quantification of new bone mineral density. Typical hematoxylin-eosin (HE) and Masson's trichrome (MT) stains of the decalcified sections also presented (x40). (b,c) Histomorphometric analysis showing the new bone length (b) and bone area (c). Data are the mean ± SD. Statistically significant difference noticed between the empty vector- and BMP-delivered groups (*P < 0.05).

We next carried out the immunohistochemical staining to examine the cellular expression of BMP2, OC, and OP proteins in the *in vivo* tissue matrix (**Fig. 11**). The BMP2 protein signal is very weak in all groups except BMP/BGN+MSC group, where the expression of BMP2 is noticed around osteoblasts and osteocytes in the newly formed bone. The signal for OC and OP protein is much clearer than that for BMP2, and the immunochemical staining is the highest in the BMP/BGN+MSC group. It is deduced that the BMP2 signal might be primarily from the cells implanted (those possibly differentiated from initial rMSCs) whereas the OCN and OPN signals could be from the extracellular molecules that are secreted from the implanted rMSCs and/or from the cells already present *in vivo*. For any reasons, the *in vivo* environments around the calvarium defect, where different sourced cells being engaged

in the bone forming process, are believed to be more favorable when the BMP/BGN transfected MSCs are implanted. The transfected MSCs can not only secret bone ECM molecules and calcify the matrix, directly forming new bone tissue, but also stimulate surrounding cells (osteoblasts or pre-existing MSCs) to get them involved in the bone forming process through paracrine effects, which yet to be clarified with further in-depth studies.

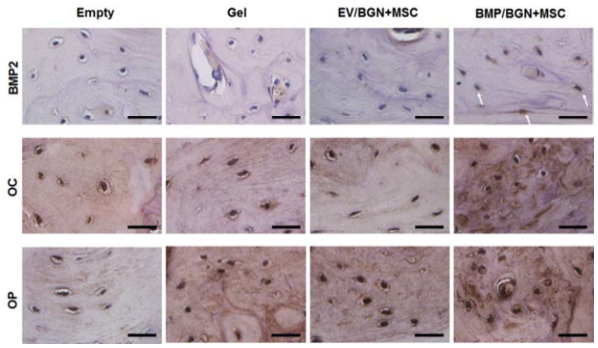

Fig. 11. Immunohistochemical expression of BMP2, OC, and OP proteins at the newly formed bone area in the calvarial defect. Note the brown coloration (white arrow) that indicates the secreted protein molecules. Stains are much clearer in OC and OP than in BMP2 (Scale bar = 25 μm).

Conclusions

A novel bioactive nanocarrier (BGN) gene delivery system was exploited for bone regeneration. The mesopores of the BGN played a significant role in effective loading and sustained delivery of the BMP2-pDNA. The delivery system could be internalized to rMSCs efficiently (over 70%), and a majority of cells were transfected to express the BMP2 protein. The osteogenic differentiation of the transfected rMSCs was demonstrated by the stimulated expression of bone markers at gene and protein levels. When implanted in a rat calvarium defect, the BMP2-pDNA/BGN delivered rMSCs showed significantly higher level of bone regeneration, in terms of bone quantity and quality. These findings support the promise of BGN-based BMP2-pDNA delivery system for effective bone regeneration, and provide a novel bioactive nanocarrier platform to advance the nanodelivery-based tissue regeneration and disease treatment of bone.

Acknowledgements

This study was supported by grants from the Global Research Laboratory (GRL) Program (No. 2015032163) and the Priority Research Centers Program (No. 2009-0093829), National Research Foundation, Republic of Korea.

Notes and references

1. L. L. Hench and J. M. Polak, *Science*, 2002, **295**, 1014-1017.
2. J. R. Jones, *Acta Biomater*, 2013, **9**, 4457-4486.
3. Q. Zhang, Y. Zhang, W. Chen, B. Zhang and S. Wang, *Exp Ther MEd*, 2013, **6**, 1443-1448.
4. A. López-Noriega, D. Arcos, I. Izquierdo-Barba, Y. Sakamoto, O. Terasaki and M. Vallet-Regí, *Chem Mater*, 2006, **18**, 3137-3144.
5. S. Jebahi, H. Oudadesse, N. Jardak, I. Khayat, H. Keskes, A. Khabir, T. Rebai, H. El Feki and A. El Feki, *Ann Pharm Fr*, 2013, **71**, 234-242.
6. K. T. Shalumon, S. Sowmya, D. Sathish, K. P. Chennazhi, S. V. Nair and R. Jayakumar, *J Biomed Nanotechnol*, 2013, **9**, 430-440.
7. H. Li, S. Chen, Y. Wu, J. Jiang, Y. Ge, K. Gao, P. Zhang and L. Wu, *Int Orthop*, 2012, **36**, 191-197.
8. N. Lindfors, P. Hyvönen, M. Nyyssönen, M. Kirjavainen, J. Kankare, E. Gullichsen and J. Salo, *Bone*, 2010, **47**, 212-218.
9. X. Liu, Z. Xie, C. Zhang, H. Pan, M. N. Rahaman, X. Zhang, Q. Fu and W. Huang, *J Mater Sci Mater Med*, 2010, **21**, 575-582.
10. M. N. Rahaman, D. E. Day, B. Sonny Bal, Q. Fu, S. B. Jung, L. F. Bonewald and A. P. Tomsia, *Acta Biomater*, 2011, **7**, 2355-2373.
11. M. Vallet-Regí, C. Ragel and A. J. Salinas, *Eur J Inorg Chem*, 2003, **2003**, 1029-1042.
12. N. L. Chacko, S. Abraham, H. N. Rao, N. Sridhar, N. Moon and D. H. Barde, *J Int Oral Health*, 2014, **6**, 20-26.
13. L. Drago, D. Romano, E. De Vecchi, C. Vassena, N. Logoluso, R. Mattina and C. L. Romano, *BMC Infect Dis*, 2013, **13**, 584.
14. C. Wu and J. Chang, *J Control Release*, 2014, **10**, 282-295.
15. S. Wang, X. Gao, W. Gong, Z. Zhang, X. Chen and Y. Dong, *Acta Biomater*, 2014, **10**, 2792-2803.
16. G. E. Vargas, L. A. Haro Durand, V. Cadena, M. Romero, R. V. Mesones, M. Mackovic, S. Spallek, E. Spiecker, A. R. Boccaccini and A. A. Gorustovich, *J Mater Sci Mater Med*, 2013, **24**, 1261-1269.
17. B. Lei, K. H. Shin, D. Y. Noh, I. H. Jo, Y. H. Koh, H. E. Kim and S. E. Kim, *Mater Sci Eng C Mater Biol Appl*, 2013, **33**, 1102-1108.
18. A. El-Fiqi, J. H. Lee, E. J. Lee and H. W. Kim, *Acta Biomater*, 2013, **9**, 9508-9521.
19. A. El-Fiqi, T. H. Kim, M. Kim, M. Eltohamy, J. E. Won, E. J. Lee and H. W. Kim, *Nanoscale*, 2012, **4**, 7475-7488.
20. E. Bergeron, M. Marquis, I. Chretien and N. Faucheux, *J Mater Sci Mater Med*, 2007, **18**, 255-263.
21. A. El-Fiqi, J. H. Kim and H. W. Kim, *ACS Appl Mater Interfaces*, 2015, **7**, 1140-1152.
22. M. S. Kang, J. H. Kim, R. K. Singh, J. H. Jang and H. W. Kim, *Acta Biomater*, 2015, **16**, 103-116.
23. Y. Z. Liu, Y. Li, X. B. Yu, L. N. Liu, Z. A. Zhu and Y. P. Guo, *Mater Sci Eng C Mater Biol Appl*, 2014, **41**, 196-205.
24. M. Vallet-Regi, I. Izquierdo-Barba and M. Colilla, *Philos Trans A Math Phys Eng Sci*, 2012, **370**, 1400-1421.
25. J. Zheng, X. Tian, Y. Sun, D. Lu and W. Yang, *Int J Pharm*, 2013, **450**, 296-303.
26. Y. Wu, D. Yang, X. Kang, P. Ma, S. Huang, Y. Zhang, C. Li and J. Lin, *Dalton Trans*, 2013, **42**, 9852-9861.

27. D. Lin, Q. Cheng, Q. Jiang, Y. Huang, Z. Yang, S. Han, Y. Zhao, S. Guo, Z. Liang and A. Dong, *Nanoscale*, 2013, **5**, 4291-4301.
28. W. Chen, P. H. Tsai, Y. Hung, S. H. Chiou and C. Y. Mou, *ACS Nano*, 2013, **7**, 8423-8440.
29. A. Z. Wilczewska, K. Niemirowicz, K. H. Markiewicz and H. Car, *Pharmacol Rep*, 2012, **64**, 1020-1037.
30. F. Tang, L. Li and D. Chen, *Adv Mater*, 2012, **24**, 1504-1534.
31. X. Wu, G. Meng, S. Wang, F. Wu, W. Huang and Z. Gu, *Mater Sci Eng C Mater Biol Appl*, 2015, **52**, 242-250.
32. R. F. De Godoy, S. Hutchens, C. Campion and G. Blunn, *J Mater Sci Mater Med*, 2015, **26**, 5387.
33. S. Murphy, A. W. Wren, M. R. Towler and D. Boyd, *J Mater Sci Mater Med*, 2010, **21**, 2827-2834.
34. P. Bosemark, H. Isaksson, M. M. McDonald, D. G. Little and M. Tägil, *Acta Orthop*, 2013, **84**, 106-111.
35. M. Draenert, K.-H. Kunzelmann, F. Forriol, R. Hickel and K. Draenert, *Bone*, 2013, **52**, 465-473.
36. M. R. Jung, I. K. Shim, H. J. Chung, H. R. Lee, Y. J. Park, M. C. Lee, Y. I. Yang, S. H. Do and S. J. Lee, *J Control Release*, 2012, **162**, 485-491.
37. X. Chen, S. Gu, B. F. Chen, W. L. Shen, Z. Yin, G. W. Xu, J. J. Hu, T. Zhu, G. Li, C. Wan, H. W. Ouyang, T. L. Lee and W. Y. Chan, *Biomaterials*, 2015, **53**, 239-250.
38. T.-H. Kim, M. Kim, M. Eltohamy, Y.-R. Yun, J.-H. Jang and H.-W. Kim, *J Biomed Mater Res A*, 2013, **101**, 1651-1660.
39. Qiao, K. Zhang, H. Jin, L. Miao, C. Shi, X. Liu, A. Yuan, J. Liu, D. Li, C. Zheng, G. Zhang, X. Li, B. Yang and H. Sun, *International journal of nanomedicine*, 2013, **8**, 2985-2995.
40. M. Wu, Q. Meng, Y. Chen, Y. Du, L. Zhang, Y. Li, L. Zhang and J. Shi, *Adv Mater*, 2015, **27**, 215-222.
41. A. Suwalski, H. Dabboue, A. Delalande, S. F. Bensamoun, F. Canon, P. Midoux, G. Saillant, D. Klatzmann, J. P. Salvetat and C. Pichon, *Biomaterials*, 2010, **31**, 5237-5245.
42. C. J. Brinker, Y. Lu, A. Sellinger and H. Fan, *Adv Mater*, 1999, **11**, 579-585.
43. M. Wang, Z. Sun, Q. Yue, J. Yang, X. Wang, Y. Deng, C. Yu and D. Zhao, *J Am Chem Soc*, 2014, **136**, 1884-1892.
44. A. Hoppe, N. S. Güldal and A. R. Boccaccini, *Biomaterials*, 2011, **32**, 2757-2774.
45. T. H. Kim, R. K. Singh, M. S. Kang, J. H. Kim and H. W. Kim, *Acta Biomater*, 2015, DOI: 10.1016/j.actbio.2015.09.035.
46. S. V. Kornilova, L. E. Kapinos and P. Blagoi Iu, *Mol Biol (Mosk)*, 1995, **29**, 574-584.
47. A. Y. Antipina and A. A. Gurtovenko, *J Phys Chem B*, 2015, **119**, 6638-6645.
48. F. Wegman, A. Bijenhof, L. Schuijff, F. C. Oner, W. J. a. Dhert and J. Alblas, *Eur Cell Mater*, 2011, **21**, 230-242.
49. J. Park, J. Ries, K. Gelse, F. Kloss, K. von der Mark, J. Wiltfang, F. W. Neukam and H. Schneider, *Gene Ther*, 2003, **10**, 1089-1098.
50. Z. K. Cui, J. Fan, S. Kim, O. Bezouglaia, A. Fartash, B. M. Wu, T. Aghaloo and M. Lee, *J Control Release*, 2015, **217**, 42-52.
51. L. Kong, C. S. Alves, W. Hou, J. Qiu, H. Mohwald, H. Tomas and X. Shi, *ACS Appl Mater Interf*, 2015, **7**, 4833-4843.
52. P. Pang, C. Wu, F. Gong, K. Zhu, X. Meng, D. Cheng, X. Hu, H. Shan and X. Shuai, *J Biomed Nanotech*, 2015, **11**, 644-656.
53. X. Yang, X. F. Walboomers, J. van den Dolder, F. Yang, Z. Bian, M. Fan and J. a. Jansen, *Tissue Eng Part A*, 2008, **14**, 71-81.
54. J. P. Fan, P. Kalia, L. Di Silvio and J. Huang, *Mater Sci Eng C Mater Biol Appl*, 2014, **36**, 206-214.